galaxies

MDPI

Article

Probing Plasma Composition with the Next Generation Event Horizon Telescope (ngEHT)

Razieh Emami [1,*], Richard Anantua [2], Angelo Ricarte [1,3], Sheperd S. Doeleman [1,3], Avery Broderick [4,5], George Wong [6,7], Lindy Blackburn [1,3], Maciek Wielgus [8], Ramesh Narayan [1,3], Grant Tremblay [1], Charles Alcock [1], Lars Hernquist [1], Randall Smith [1], Matthew Liska [1], Priyamvada Natarajan [3,9], Mark Vogelsberger [10], Brandon Curd [1,3] and Joana A. Kramer [8]

1 Center for Astrophysics | Harvard & Smithsonian, 60 Garden Street, Cambridge, MA 02138, USA
2 Department of Physics & Astronomy, The University of Texas at San Antonio, One UTSA Circle, San Antonio, TX 78249, USA
3 Black Hole Initiative, Harvard University, 20 Garden Street, Cambridge, MA 02138, USA
4 Perimeter Institute for Theoretical Physics, 31 Caroline Street North, Waterloo, ON N2L 2Y5, Canada
5 Department of Physics and Astronomy, University of Waterloo, 200 University Avenue West, Waterloo, ON N2L 3G1, Canada
6 School of Natural Sciences, Institute for Advanced Study, 1 Einstein Drive, Princeton, NJ 08540, USA
7 Princeton Gravity Initiative, Princeton University, Princeton, NJ 08544, USA
8 Max Planck Institute for Radio Astronomy, Auf dem Huegel 69, D-53121 Bonn, Germany
9 Departments of Astronomy & Physics, Yale University, New Haven, CT 06511, USA
10 Department of Physics, Kavli Institute for Astrophysics and Space Research, Massachusetts Institute of Technology, Cambridge, MA 02139, USA
* Correspondence: razieh.emami_meibody@cfa.harvard.edu

Abstract: We explore the plasma matter content in the innermost accretion disk/jet in M87* as relevant for an enthusiastic search for the signatures of anti-matter in the next generation of the Event Horizon Telescope (ngEHT). We model the impact of non-zero positron-to-electron ratio using different emission models, including a constant electron to magnetic pressure (constant β_e model) with a population of non-thermal electrons as well as an R-beta model populated with thermal electrons. In the former case, we pick a semi-analytic fit to the force-free region of a general relativistic magnetohydrodynamic (GRMHD) simulation, while in the latter case, we analyze the GRMHD simulations directly. In both cases, positrons are being added at the post-processing level. We generate polarized images and spectra for some of these models and find out that at the radio frequencies, both of the linear and the circular polarizations are enhanced with every pair added. On the contrary, we show that, at higher frequencies, a substantial positron fraction washes out the circular polarization. We report strong degeneracies between different emission models and the positron fraction, though our non-thermal models show more sensitivities to the pair fraction than the thermal models. We conclude that a large theoretical image library is indeed required to fully understand the trends probed in this study, and to place them in the context of a large set of parameters which also affect polarimetric images, such as magnetic field strength, black hole spin, and detailed aspects of the electron temperature and the distribution function.

Keywords: M87*; plasma composition; EHT; ngEHT

Citation: Emami, R.; Anantua, R.; Ricarte, A.; Doeleman, S.S.; Broderick, A.; Wong, G.; Blackburn, L.; Wielgus, M.; Narayan, R.; Tremblay, G.; et al. Probing Plasma Composition with the Next Generation Event Horizon Telescope (ngEHT). *Galaxies* **2023**, *11*, 11. https://doi.org/10.3390/galaxies11010011

Academic Editor: Bidzina Kapanadze

Received: 14 November 2022
Revised: 27 December 2022
Accepted: 4 January 2023
Published: 10 January 2023

1. Plasma Composition: Observational Studies

Large scale jets are launched and are collimated by their surrounding accretion flow through extracting the black hole rotational energy by purely electromagnetic mechanisms [1–5]. At radio frequencies, jets are visible from the sub-pc to the kpc scales through the synchrotron emission from the ultra-relativistic electrons gyrating inside the magnetic field. Consequently, jets link the accretion physics to the particle acceleration [6,7]. On the theoretical front, significant progress has been made most recently in modeling the jet formation and

its morphology where the current GRMHD simulations are able to recover the observed Lorentz factor. There are many factors that contribute to the jet formation, collimation, acceleration and propagation. Of key importance is the matter content of the jet; either in terms of the normal plasma (composed of electron-protons) or the pair plasma (composed of electron-positron pairs), they lead to very distinct observational signatures. Recently, there have been some theoretical studies [8,9] on probing the observational signatures of different plasma components.

Despite the fundamental importance of plasma composition, up until now, there have not been any conclusive observations that clearly favor either normal or pair plasma. Below, we mention a few different efforts.

Radio-loud quasars and the active galactic nuclei (AGN) make roughly 10% of the population of jets and exhibit very powerful jets, propagating hundreds of kpc away before being disrupted [10]. Consequently, they can be good candidates for searching the matter content of the jet.

Giant elliptical galaxy M87 at the center of the Virgo cluster contains a very spectacular extragalactic jet (firstly discovered by [11]), with a relatively low radio luminosity. The synchrotron and the inverse Compton emissions from the jet bases produce radiation at other frequencies including the optical, X-rays and the γ-rays far outside the host galaxy. Consequently, M87 has been subject to wide studies at multi-frequencies from the radio to γ-rays [12], as well as the *X*-rays [13]. Furthermore, an extended study has also been conducted on its jet collimation using the Very Long Baseline Interferometry (VLBI) at sub-millimeter wavelengths [14–22]. The synchrotron spectrum of M87 jet was first studied in [23]. The combination of all of these studies makes M87 a very valuable source to probe the matter content of the jet.

Reynolds et al. [10] used the historical data from the VLBI observations of M87 at 5 GHz and probed the physical properties of the jet as well as its matter content using the synchrotron self-absorption theory [6] relevant for the radio emission from the compact core of M87. They put constraints on the magnetic field and the particle density of the jet and eventually on the matter content of the jet. Their results strongly favored a pair dominated plasma; although, they did not yet rule out the possibility of a normal plasma. As they argued, a multi-frequency analysis of the jet may unambiguously put constraints on the matter content of the jet.

The quasar 3C279 is another example of a luminous object in the sky, located at redshift $z = 0.538$, already observed with the EHT [24]. It is luminous from radio to γ-ray wavelengths. At the radio frequency, the VLBI observations demonstrate a very bright and unresolved core along with a jet extended to the kpc scales. There are superluminal motions associated with this source in the jet, with velocities raging from 4–15 times the speed of light, indicating a relativistic bulk speed in the jet. Consequently, the emitted radiation from the jet at different wavelengths are boosted by the Doppler effect. Owing to its relatively high flux, 3C279 is an ideal source to probe the physics of the extragalactic source. To probe the jet decomposition in quasar 3C279, [25] used the circular polarization from the observations of 3C279 at 15 GHz. The circular polarization is produced through the Faraday conversion, requiring the energy distribution of particles being extended to lower energies. Combining their final results with other extragalactic sources, such as M87, they concluded that, in general, the extragalactic jets might be primarily composed of pairs. Furthermore, they argued that since the jet densities should be rather low, the pair-dominated jet points us to a picture in which photon cascades or the Pion decay are the main origin of the radiating particles in the jet.

The quasar 3C345 at redshift $z = 0.594$ is a core-dominated radio source with a prominent pc-scale jet, emitting X-rays through the Synchrotron self-Compton (SSC) process. This source has been monitored at 5 GHz every year since 1977. Higher frequency monitoring of this source, at both 10.5 and 22 GHz, are conducted more frequently. [26] combined the constraints on the electron number density from the Synchrotron Self-Absorption with the

kinetic luminosity constraints and concluded that C2, C3, C4, C5 and C7 components of quasar 3C345 are predominantly made of pairs rather than normal plasma.

Despite the fact that in all of the above sources probed using the aforementioned methods, pair plasma is favored against the normal plasma; this conclusion does not hold for other sources. For example, the radio galaxy 3C 120, located at $z = 0.033$, presents a strong interaction between the jet and its interstellar cloud in which the matter content of the jet is mixed with the dense surrounding thermal gas. If the jet in this source is mostly composed of pairs, their positrons would enter the cloud and be thermalized through the ionized energy lost. The annihilation rate of such positrons in the cloud would then have to be proportional to the positron density of the jet. The observations of narrow emission lines would then inform us about the matter content of the jet. [27] made an exploration of the matter content of the jet in this source through their annihilation line flux, using the hard X-ray and soft γ-ray spectrum from the SPI spectrometer on INTEGRAL. Their spectral analysis failed to detect any lines and thus could not consistently constrain the positron to electron ration in this source.

More statistically, Ref. [28] used a sample of radio-load quasars and addressed the puzzle of plasma matter content. Out of the possibility of a normal or a pair plasma and based on the annihilation constraints, combined with the assumption that pairs are originated from the inner part of the accretion, they favored an electron-proton plasma.

In summary, there are some controversial results in the observational searches for the plasma matter content. Consequently, the key question of the plasma matter content remains elusive.

Being mindful of the current status of searches for positrons, in what follows, we review different theoretical studies that motivate a pair plasma. We will then focus on two sets of toy models, one based on a semi-analytic type of models, while the other from the GRMHD simulations. In the latter case, we make the polarized images for one snapshot. Work is in progress to extend this analysis to the case with a time-averaged polarized image set for GRMHD simulations. In both cases, we add positrons at a post-processing level using different ray-tracing codes. We apply the most recent polarimetric constraints, on the fractional linear polarization, from the EHTC [29,30] and put constraints on the plasma matter contents.

The paper is organized as follows. Section 2 reviews theoretical approaches in making the pair-plasma. Section 3 describes the radiative transfer approach in making the polarized images of BH. Section 4 models the impact of positrons in a semi-analytic approach. Section 5 introduces a GRMHD method to deal with the impact of positrons. Section 6 provides a conclusion of the paper.

2. Theoretical Approaches in Creating Pairs

There are two distinct classes of models which lead to pair creation through photon annihilation, known as the Briett-Wheeler process [31]. The electron-positron pairs could either be created from a coherent, steady state and large-scale mechanisms (as relevant in the gap systems) [32–37] or, rather, originate from an incoherent, transient and small-scale approach (being appropriate in pair drizzle systems) [38]. However, while in the gap approach, the high energy photons have an energy orders of magnitude above the rest-mass energy of electrons ($\simeq$MeV); in the pair drizzle approach, the host photons have an energy of roughly MeV. Despite the distinct features of the gap and drizzle models, they could be thought of as the continuum distribution in two different ends for the energy spectrum of the created photons.

In the following, we review these scenarios in more depth:

1. Gap models make high-energy photons in coherent regions with $\mathbf{E} \cdot \mathbf{B} \neq 0$, which accelerate the leptons and make the pair cascades. Broderick and Tchekhovskoy [39] showed that the stagnation surface, in these gap models, defined as the boundary between the material falling back to the black hole and outflows (forming the jet), would be a natural site for the pair creation followed by the particle acceleration. They showed that un-

screened electric fields lead to the production of photons from the accretion flow, inside the jet. These photons would then make non-thermal particles through their inverse Compton scattering. As they argued, this method leads to a population of non-thermal particles consistent with the most recent sub mm-VLBI observations of M87. In this method, there are two distinct mechanisms in making/propagating the pairs. In the gap region, particles are highly accelerated, limited by the inverse Compton cooling, followed by the net charge separation. They emit photons, which then make electron-positron pairs through the Compton scattering off the ambient soft photons. In this picture, particles moving inward are accreted by the central BH while those travelling outward are making the jets. In such spark gaps, positron densities may exceed the Goldreich-Julian value required to screen electric fields, limiting the efficiency of pair cascades once enough positrons are formed.

2. Pair drizzle models predict a steady and smooth background population of photons, being created from the high-energy part of electron distribution function in the near horizon plasma. Such $\sim$ MeV photons make e^-/e^+ pairs throughout their interactions. Mościbrodzka et al. [38] estimated the pair creation rate based on the non-relativistic GRMHD simulations. Wong et al. [40] extended this approach to include a radiative-based GRMHD simulation from `ebh-light` code [41–43]. They used an axisymmetric model and explored different mass accretion rates corresponded to an optically thin and geometrically thick accretion flow of SANE simulation. Figure 1 presents the logarithmic ratio of available pair to the Goldreich-Julian density (see Equation (33) of [40] for more details) (left panel) for a GRMHD model with $a = 0.5$ with the accretion rate $\dot{m}/\dot{M}_{\rm Edd} = 1.1 \times 10^{-5}$. In the left panel, it is evident that the available pair ratio is much above unity in the disk and in the funnel jet, demonstrating that these locations might be a good site for pairs to appear. The right panel also shows the logarithmic rate of the pair production density in the same model. It is seen that the rate of pair production is enhanced in the inner part of the disk and in the equatorial plane, but diminishes significantly at larger radii, e.g. $x > 5{\rm GM/c^2}$ as well as the high scale heights, e.g. $z > 3{\rm GM/c^2}$.

Consequently, we conclude that while in gap models, pairs are being mostly created in the jet funnel, pair drizzle models make them more in the accretion disk.

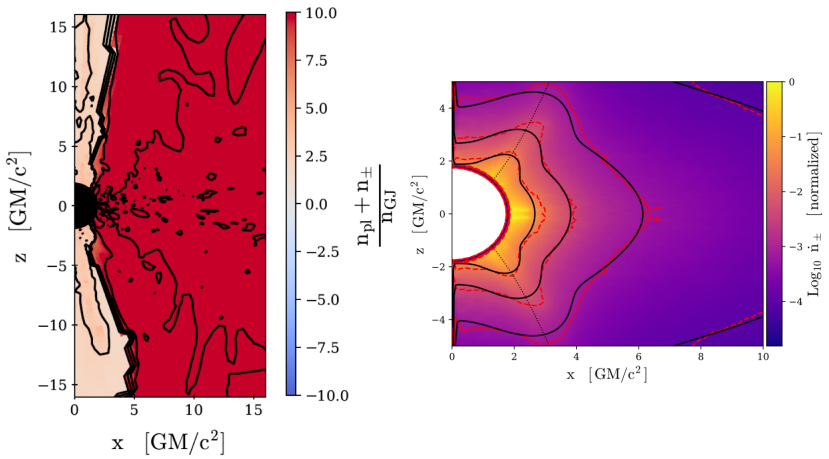

Figure 1. (**Left panel**) The ratio of the available pair density to the Goldreich-Julian density for a GRMHD simulation model with a = 0.5. (**Right panel**) The time-averaged logarithmic rate of the pair production density taken from [40] as a function of the position. In each panel, the horizontal axis presents the radial coordinate while the vertical axis shows the height above the disk mid-plane. From the plot, it is inferred that the pair production rate is enhanced in the inner part of the accretion disk and in the equatorial plane. Dashed red lines and solid black lines compare the numeric and the fits to the contours of the rate of the number density. See [40] for more details.

3. Radiative Transfer of Pair Plasma

Due to their opposite charge, positrons gyrate in a magnetic field in the opposite direction to electrons. This has significant effects on the radiative transfer coefficients, namely the synchrotron emission/absorption and Faraday rotation. Compared to an ionic plasma, a pair plasma produces no Faraday rotation, nor does it produce any circular polarization from synchrotron radiation. On the other hand, linear polarization emission and Faraday conversion persist. Consequently, polarization can be used to place constraints on the plasma composition and has fuelled a decades-long debate about the composition of astrophysical jets [6,25,44].

In general relativistic radiative transfer GRRT, the radiative transfer coefficients (see e.g., [45], for their derivation and definitions) are modified via:

$$\begin{aligned} j_{I,Q,U} &\to (1+f_{\rm pos}) j_{I,Q,U}, \\ j_V &\to (1-f_{\rm pos}) j_V, \\ \alpha_{I,Q,U} &\to (1+f_{\rm pos}) \alpha_{I,Q,U}, \\ \alpha_V &\to (1-f_{\rm pos}) \alpha_V, \\ \rho_{Q,U} &\to (1+f_{\rm pos}) \rho_{Q,U}, \\ \rho_V &\to (1-f_{\rm pos}) \rho_V. \end{aligned} \tag{1}$$

where j_i and α_i are the emission and absorption coefficients, ρ_i refer to the rotativities, and $f_{\rm pos}$ describes the positron-to-electron ratio. Qualitatively, increasing the positron fraction tends to increase the linear polarization fraction by reducing the Faraday rotation depth. The circular polarization fraction and the image morphology may also change significantly as the balance between circular polarization generated by emission and Faraday conversion changes. Since the Faraday conversion, Faraday rotation, and circular polarization emission coefficients evolve differently with the frequency, this may lead to large changes in the polarized spectrum. Consequently, a multi-frequency analysis might be very helpful in putting constraints on the plasma composition.

Below, we use the above prescription and analyze the impact of positrons in polarized images from a semi-analytical model in Section 4 as well as two sets of GRMHD simulation in Section 5. As we will describe, in both cases, we have added the positrons at the ray-tracing level by the aforementioned algorithm. Throughout our analysis, we focus on M87*.

4. Positron Effects in the Semi-Analytical Models

To probe the observational signatures of a pair plasma in the polarized emission from the jet/accretion in M87*, we make use of a semi-analytical approach [9], as a self-similar jet model focusing on the force-free regions of a Blandford-Znajek outflow model in [8,46] with several extensions including a general relativistic ray-tracing from the GRTRANS code [45], as well as the usage of non-thermal distribution to describe the number density of pairs. In this model, the number density of pairs is mapped to total electron/positron pressure, with an overall electron to magnetic pressure β_e. Furthermore, we assume a self-similar parabolic jet profile $\xi = s^2/z$, in the cylindrical coordinate. We use some fitting formulae for the ξ, using the magnetic flux $\Phi_B(\xi)$, the line angular speed $\Omega_B(\xi)$ and the velocity component along with the z-coordinate, $v_z(\xi)$ being extracted from a `HARM` simulation [47]. In more detail, for the GRMHD, we use a magnetically arrested disk (MAD) simulation with $a/M = 0.92$ and infer the fitting formulas at $z = 50M$. Note that these models are idealized and axis-symmetric, and polarized signatures are sensitive to additional parameters, including spin, magnetic field state, and the electron-to-ion temperature ratio [30]. Nevertheless, this simple model can be used to explore and illustrate the qualitative changes as positrons are added to the accretion flow.

Next, we extrapolate these quantities to larger radii, taking advantage of the self-similarity in ξ; see Equations (18)–(26) of [9] for more details.

As already mentioned above, we use a non-thermal, power-law distribution for the emitting electrons, with a Lorentz factor between $\gamma_{\rm min}$ and $\gamma_{\rm max}$:

$$N_{e^-}(\gamma) = \begin{cases} N_0 \gamma^{-p} & \gamma_{\rm min} \leq \gamma \leq \gamma_{\rm max} \\ 0 & \text{otherwise} \end{cases}, \quad (2)$$

where $N_0 = n_{e^-}(p-1)/\left(\gamma_{\rm min}^{1-p} - \gamma_{\rm max}^{1-p}\right)$ refers to the overall normalization of the electron distribution and with n_{e^-} describing the total number density of electrons as given by Equation (28) of [9]. We implement this model to GRTRANS, modifying its equations for the emissivity, absorption and the Faraday terms to include the contribution of positrons. Below, we describe the results including the polarized images, the spectra and the multi-frequency analysis.

4.1. Polarized Images

In what follows, we compare polarized intensity maps of models with varying ratios n_{e+}/n_0 of added electron-positron pairs to original plasma electrons and mechanisms for accelerating electrons and positrons to relativistic speeds such that they radiate synchrotron radiation at 230 GHz. The color maps show the 230 GHz flux (intensity times solid angle of a pixel) for total intensity I, linearly polarized intensity P and circularly polarized intensity V for synthetic images of our emission models. The polarization serves as a key discriminant for degenerate total intensity images whose electrons and positrons contribute differently to intrinsic circular polarization and Faraday rotativity radiative transfer coefficients.

Figure 2 presents the polarized image of the constant β_e model at 230 GHz for the case with no positrons (top panel) and the one with 50% of positrons (bottom panel). (Note the circularly polarized 230 GHz intensities are shown in terms of the brightness temperature T_b that a black-body would possess to give the same luminosity volumetrically as the maps display at the observed frequency.)From the plot, it is seen that, in this model, adding the positrons significantly increases the linear and the circular polarization. Consequently, we expect that the EHT polarimetric constraints disfavor the case with significant pair fraction in the constant β_e model.

Next, we explore the impact of changing the parameters of the emission model. Figures 3 and 4 show the linear and circular polarization maps for different models' parameters. In each figure, in the top panel, we change $\beta_e = 10^{-6}, 10^{-4}, 10^{-1}$, while in the bottom row, we alter the slope $p = 2.5, 3.0, 3.5$, while fixing $f_{\rm pos} = 0.1$.

From the plots, it is inferred that increasing the β_e as well as p suppress the linear and circular polarization, since increasing the β_e and p enhances the Faraday rotation, which itself leads to scrambling of the EVPA and, thus, the suppression of the linear and the circular polarization. In [9], we made an in-depth exploration of the impact of changing the β_e and non-thermal power-law slope p on the SED, see Figures 9 and 11 of [9] and tables 2 and 4 for more details. Finally, it is seen that the shape of the circular polarization also changes when we vary the parameters of the emission model. This implies that a direct detection of the circular polarization map might be useful to break the degeneracy between the physical parameters of the model as well as the matter content of the emitting plasma.

We emphasize that the polarization maps here use the standard EHT point spread function based on a 20 μ as beam. However, ngEHT may be able to focus on half this scale, In [48], intensity maps are shown to possess higher maxima when they are more highly resolved owing to an increase in pixels per plane. The effect of partitioning the intensity into refined bins can also slightly shift the location of intensity maxima. These trends hold for the polarized images as well.

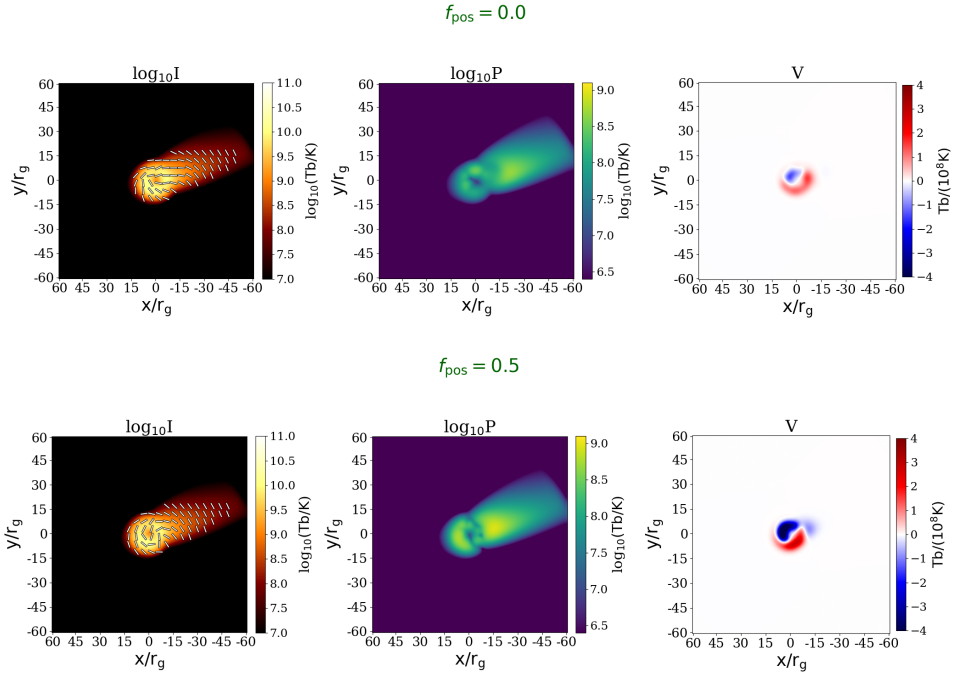

Figure 2. Down rows present the polarized map of M87* inferred from the constant β model at 230 GHz. We have fixed $\beta_e = 0.01$, and the power-law index at $p = 3.5$. From the (**top**) to (**bottom**), we present the images for $f_{\rm pos} = 0.0, 0.5$, respectively.

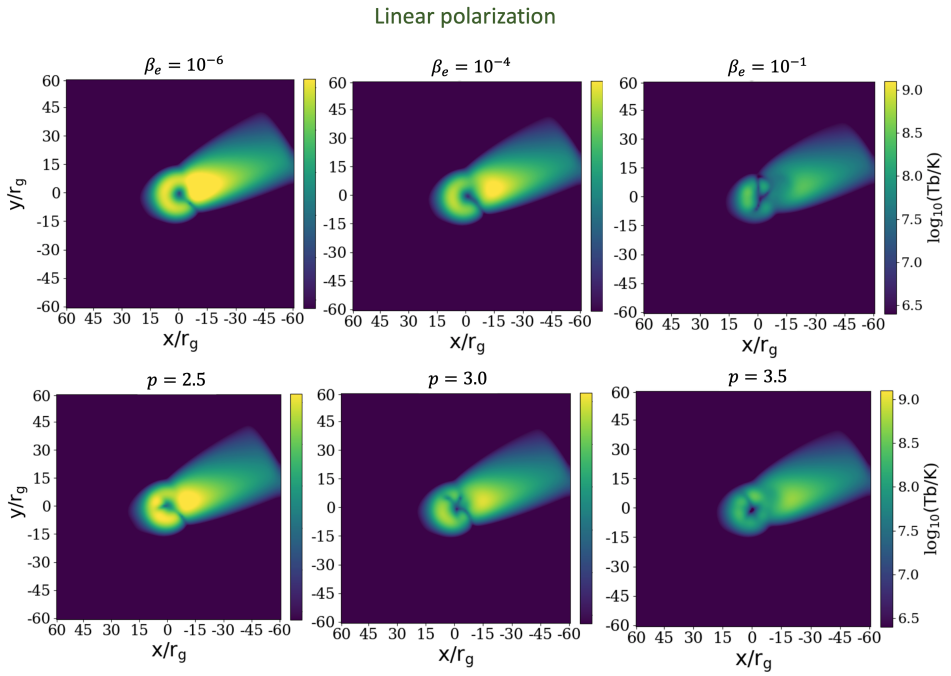

Figure 3. The (log)-linear polarization map for the constant β model with $f_{\rm pos} = 0.1$. (**Top panel**) shows the case with $p = 3.5$. From the left to right we change $\beta_e = 10^{-6}, 10^{-4}, 10^{-1}$. (**Bottom panel**) presents the case with fixed $\beta_e = 10^{-2}$, also from the left to right, we change p = (2.5, 3.0, 3.5). These images are corresponded to $\nu = 230$ GHz.

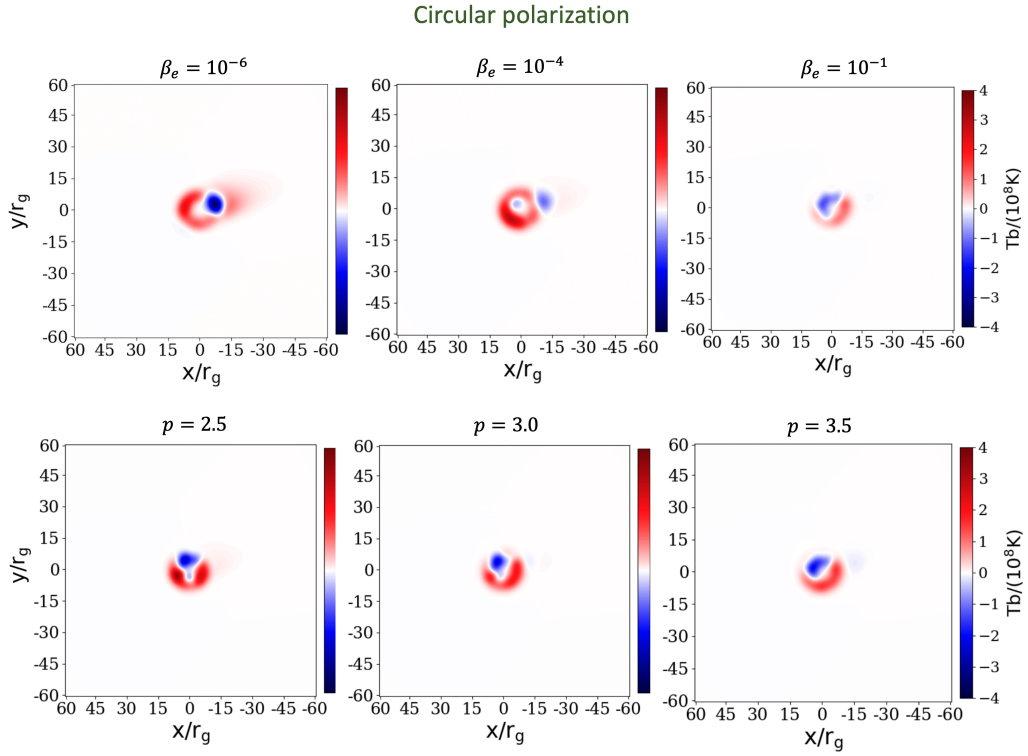

Figure 4. The circular polarization map for the constant β model with $f_{\rm pos}$ = 0.1. (**Top panel**) shows the case with p = 3.5. From the left to right we change $\beta_e = 10^{-6}, 10^{-4}, 10^{-1}$. (**Bottom panel**) presents the case with fixed $\beta_e = 10^{-2}$, also from the left to right, we change p = (2.5, 3.0, 3.5). These images are corresponded to $\nu = 230$ GHz.

4.2. Spectral Analysis

In Figure 5, from the left to right panels, we analyze the spectrum of the total intensity, the linear and circular polarization, respectively. Motivated by a wide model survey performed in [9] and since $\beta_e = 10^{-2}$ and $p = 3.5$ perform well in satisfying the EHT polarimetric results, we choose these values and only vary the $f_{\rm pos} = (0.0, 0.1, 1.0)$. Overlaid in each panel, we present the observational data points from [49–51] as well as the most recent results from the EHT observation [9,30]. Furthermore, we fix the model parameters to match the observed flux at ν = 230 GHz. Consequently, the impact of fluid composition is somewhat renormalized to get the flux right and, thus, does not have any other impact on the total flux at 230 GHz.

As expected, the total flux (left panel) is off at higher frequencies. This implies that, while the current toy model describes the radio observations quite well, a more complicated model would be required to match the flux at higher frequencies.

The fractional linear polarization, from the middle panel, shows more sensitivity to altering the positron fraction. Based on our simple semi-analytic model, it is inferred that models with higher $f_{\rm pos}$ sit above the current EHT constraints. In Emami et al. [9], we made a detailed survey of different models and realized that varying the β_e and p do not change the above conclusion, implying that there are severe constraints for the constant β_e model. However, we emphasize that this conclusion may not be easily generalized to other accretion flow models. For example, as we will see below, certain thermal models provide less severe constraints.

Finally, the circular polarization, in the right panel, establishes more interesting dependencies to the positron fraction. It is explicitly seen that circular polarization is not only too sensitive to the positron fraction at the radio frequencies, but it also shows distinct features at higher frequencies. Consequently, a multi-frequency analysis should break the degeneracies in searching for positrons. While the current polarimetric results only cover

230 GHz, we hope that adding more frequencies to the ngEHT improves these constraints further. In the next section, we briefly discuss this while leaving an in-depth analysis to a future work.

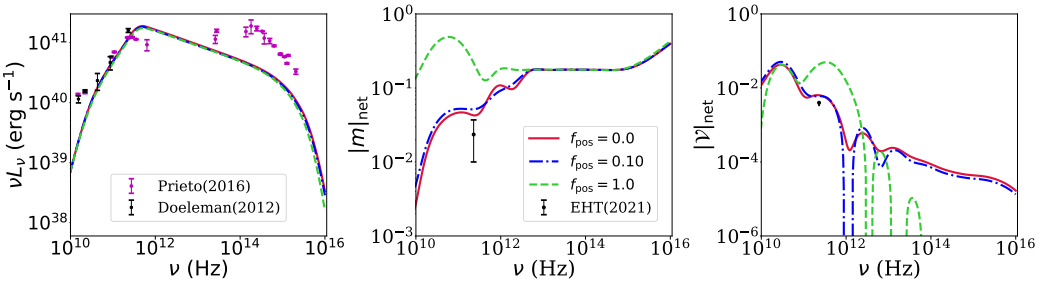

Figure 5. The spectrum of the best bet model for the jet model [9] with $\beta_e = 10^{-2}$ and $p = 3.5$. From the (**left**) to (**right**), we present the total intensity, the linear and the circular polarization, respectively. Overlaid on each panel, we also present the observational data points.

4.3. Multi-Frequency Analysis

In Figure 6 down rows present a multi-frequency image analysis; the top, middle and bottom rows present 86, 345 and 690 GHz, respectively. In each row, from the left to right, we present the intensity, linear and the circular polarizations. From the plot, it is inferred that increasing the frequency washes out the linear and circular polarization substantially. Furthermore, the image is also core shifted at higher frequencies where the larger-scale patterns in the electric vector polarization angles (EVPAs) are boosted to the central part of the image. Finally, the shape of the circular polarization is also altered at higher frequencies. As the morphology of the polarized images strongly depends on the frequency, a simultaneous observation at the above frequencies would be very capable of breaking the model degeneracies. Consequently, we propose to use the ngEHT to break the model degeneracies.

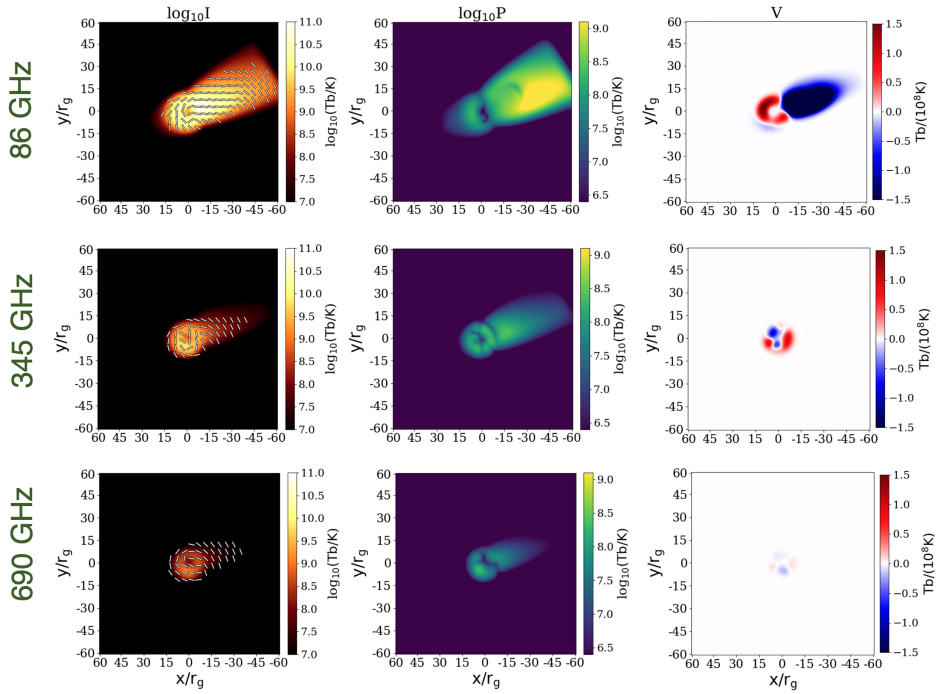

Figure 6. Down rows present the polarized map ((**left**) to (**right**) the intensity, linear and circular polarization) of M87* in constant beta model at 86, 345 and 690 GHz, respectively. The plot is for $f_{pos} = 0.1$, $p = 3.5$ and $\beta = 10^{-2}$.

5. Positrons in GRMHD KHARMA Simulation

Next, we generalize the above semi-analytic approach to a direct GRMHD simulation approach (Anantua et al. in prep.), where positrons are still being added during a post-processing step to KHARMA simulation [52]. These simulations are run assuming an adiabatic index of 5/3, although there is no evidence that changing the adiabatic index to values as low as 4/3 significantly impacts our images. While an in-depth analysis of the impact of positrons is left to a separate work, here we aim to take the first look at the possible importance of changing the accretion type as well as the electron emission profiles from non-thermal models to that of thermal models.

In Figures 7 and 8, we present a MAD model with $a = 0.94$ and a SANE model with $a = +0.5$, respectively. In both of these figures, we use a familiar turbulent heating-based emission model in which the ion-to-electron temperature ratio $R = (1+\beta^2)^{-1}R_{\rm low} + \beta^2(1+\beta^2)^{-1}R_{\rm high}$ approaches parametrically determined values $1/R_{\rm low}$ in the low=β polar outflow and $1/R_{\rm high}$ in the high-β accretion disk. More explicitly, we choose, $R_{\rm low} = 1$ and $R_{\rm high} = 20$. It is seen that the addition of positrons (where electron-positron pair number density $n_{\rm pair}$ is varied relative to the original electron number density n_0) has remarkably little effect on the linear polarization pattern. A more significant difference is seen in circular polarization, however, which historically has been promising to use to test plasma composition models [25]. This is because only ionic plasma can produce the circular polarization via direct synchrotron emission, and a pair plasma does not perform Faraday rotation, which can affect linear polarization that goes through Faraday conversion [44]. Since large-scale circularly polarized emission originates from direct synchrotron in this model [53], the large-scale emission disappears when a significant population of pairs is added. Note that polarized EHT observations at present only weakly and indirectly constrain spin, using models without positrons; so, we explore several different values in this text [30]. In the top row, we show the result of a normal ray tracing, without the addition of pairs, using IPOLE [54], while in the bottom one, we present the case with 100 times more electron-positron pairs, added at a post-processing level, to the pre-existing electron number density in KHARMA GRMHD simulation. This approximates a full pair plasma while preserving charge neutrality. From left to right, different columns present the total intensity, linear and the circular polarization, respectively.

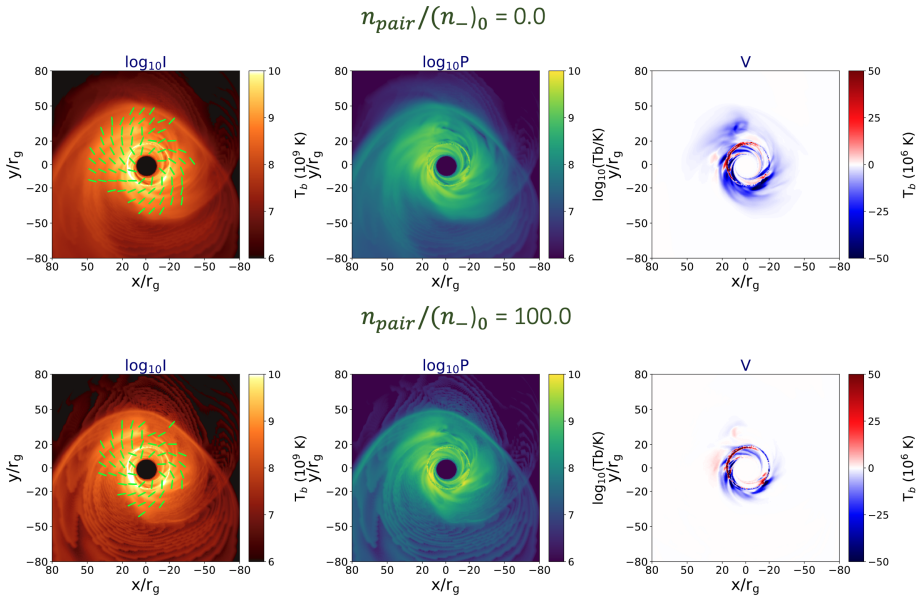

Figure 7. A map from MAD simulations with a = +0.94 at $R_{\rm high}$ = 20 in R-beta model from KHARMA simulations. The top row refers to the case with no positrons while the bottom one describes the case with 100% positrons compared with the original number of electrons. In each row, from the (**left**) to (**right**), we present the images of total intensity, the linear and the circular polarization, respectively. We have used ν = 230 GHz to make these images.

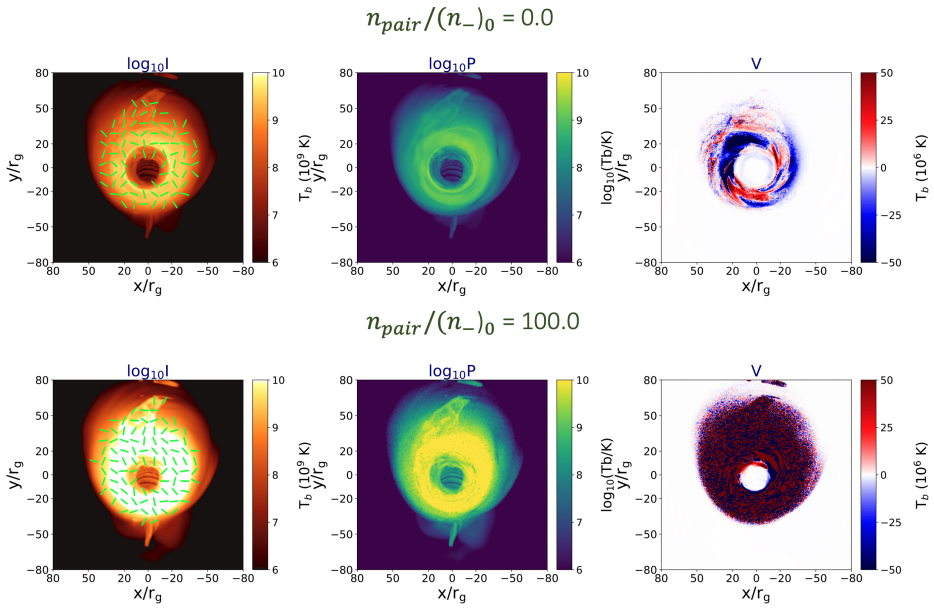

Figure 8. A map from SANE simulations with a = +0.5 at $R_{\rm high}$ = 20 in R-beta model from KHARMA simulations. The top row refers to the case with no positrons while the bottom one describes the case with 100% positrons compared with the original number of electrons. In each row, from the (**left**) to (**right**), we present the images of total intensity, the linear and the circular polarization, respectively. We have used ν = 230 GHz to make these images.

In Figure 8, we see that the linear polarization pattern of the SANE model is much more strongly affected by the addition of pairs than in the MAD model. This is because the model is intrinsically Faraday-thick, resulting in a significant scrambling. The addition of pairs dramatically decreases the Faraday depth, resulting in an ordered linear polarization pattern. Faraday rotation may also have an indirect effect on circular polarization by scrambling the linear polarization that would be transformed into circular polarization. As we see here, the addition of pairs dramatically increases the resolved circular polarization by removing this scrambling effect.

Comparing the current GRMHD simulation results with that of Section 4, it is inferred that changing the emission model significantly affects the morphology of the polarized images.

6. Conclusions

There have been many outstanding observational claims for a substantially pair-dominated plasma in the radio-load quasars and in AGNs. Motivated by this, in this manuscript, we studied the theoretical signatures of having non-zero positrons in the polarized images in a force-free, semi-analytic jet model (Section 4) as well as a snapshot of the KHARMA GRMHD simulations (Section 5), where in both cases, positrons are added at the post-processing level. While the Faraday rotation diminishes by increasing the positron fraction, the Faraday Conversion is boosted linearly. We showed that the role of positrons is also mixed with different emission models in a degenerate picture. A multi-frequency analysis in the radio band, 86–690 GHz as relevant for the ngEHT, or a much wider frequency search in the near infrared and the X-ray, may however break the degeneracy. Increasing the frequency, there is a core shift in images that wash out the power at larger scales and squeeze them more to the central part of the image. Consequently, we argue that lower frequencies may give rise to a better chance to search for positrons. Therefore, 86 or 230 GHz from the ngEHT could be very relevant frequencies for looking for a pair plasma in the heart of M87*. Finally, we emphasize that the positron fraction is just one of many physical parameters that affect the polarized images. In a future work, we aim for a broader investigation including a large image library probing different GRMHD models and emission prescriptions to determine how well these results may be generalized.

Author Contributions: Conceptualization, R.E., R.A., A.R., S.S.D., A.B., M.V., P.N., B.C., J.A.K. Methodology, R.E. Software, R.E., R.A., A.R. Validation, R.E. Formal analysis, R.E., R.A., A.R. Investigation, R.E., G.W., M.W., Resources, R.A., A.R. Data curation, R.E., R.A., G.W. Writing, R.E., R.A., A.R., M.W., L.B. Original draft preparation, R.E. Review and editing, R.E., R.A., A.R., M.W. Supervision, S.S.D., R.N., G.T., C.A., L.H., R.S., M.L. Funding, R.N., G.T., R.S., M.L. All authors have read and agreed to the published version of the manuscript.

Funding: Razieh Emami acknowledges the support of the Institute for Theory and Computation at the Center for Astrophysics as well as grant numbers 21-atp21-0077, NSF AST-1816420 and HST-GO-16173.001-A for their very generous support. This work was supported in part by the Black Hole Initiative, which is supported by grants from the Gordon and Betty Moore Foundation and the John Templeton Foundation. The opinions expressed in this publication are those of the author(s) and do not necessarily reflect the views of the Moore or Templeton Foundations.

Data Availability Statement: The data presented in this study are available on request from the corresponding author.

Acknowledgments: We greatly appreciate positrons for most likely making the AGN jets and we wish to discover them using the ngEHT! Special thanks to the referees as well for very constructive comments.

Conflicts of Interest: The authors declare no conflict of interest.

References

1. Blandford, R.D.; Znajek, R.L. Electromagnetic extraction of energy from Kerr black holes. *Mon. Not. R. Astron. Soc.* **1977**, *179*, 433–456. [CrossRef]
2. Tchekhovskoy, A.; Narayan, R.; McKinney, J.C. Black Hole Spin and The Radio Loud/Quiet Dichotomy of Active Galactic Nuclei. *Astrophys. J.* **2010**, *711*, 50–63.
3. Tchekhovskoy, A.; Narayan, R.; McKinney, J.C. Efficient generation of jets from magnetically arrested accretion on a rapidly spinning black hole. *Mon. Not. R. Astron. Soc.* **2011**, *418*, L79–L83,
4. Tchekhovskoy, A.; McKinney, J.C. Prograde and retrograde black holes: whose jet is more powerful? *Mon. Not. R. Astron. Soc.* **2012**, *423*, L55–L59.
5. Tchekhovskoy, A. Launching of Active Galactic Nuclei Jets. In *The Formation and Disruption of Black Hole Jets*; Astrophysics and Space Science Library; Contopoulos, I., Gabuzda, D., Kylafis, N., Eds.; Springer: Cham, Switzerland, 2015; Volume 414, p. 45. [CrossRef]
6. Blandford, R.D.; Königl, A. Relativistic jets as compact radio sources. *Astrophys. J.* **1979**, *232*, 34–48. [CrossRef]
7. Blandford, R.D.; Payne, D.G. Hydromagnetic flows from accretion disks and the production of radio jets. *Mon. Not. R. Astron. Soc.* **1982**, *199*, 883–903. [CrossRef]
8. Anantua, R.; Emami, R.; Loeb, A.; Chael, A. Determining the Composition of Relativistic Jets from Polarization Maps. *Astrophys. J.* **2020**, *896*, 30.
9. Emami, R.; Anantua, R.; Chael, A.A.; Loeb, A. Positron Effects on Polarized Images and Spectra from Jet and Accretion Flow Models of M87* and Sgr A*. *Astrophys. J.* **2021**, *923*, 272,
10. Reynolds, C.S.; Fabian, A.C.; Celotti, A.; Rees, M.J. The matter content of the jet in M87: evidence for an electron-positron jet. *Mon. Not. R. Astron. Soc.* **1996**, *283*, 873–880.
11. Curtis, H.D. The Planetary Nebulae. *Publ. Lick Obs.* **1918**, *13*, 55–74.
12. Abramowski, A.; Acero, F.; Aharonian, F.; Akhperjanian, A.G.; Anton, G.; Balzer, A.; Barnacka, A.; Barres de Almeida, U.; Becherini, Y.; Becker, J.; et al. The 2010 Very High Energy γ-Ray Flare and 10 Years of Multi-wavelength Observations of M 87. *Astrophys. J.* **2012**, *746*, 151,
13. Biretta, J.A.; Stern, C.P.; Harris, D.E. The Radio to X-ray Spectrum of the M87 Jet and Nucleus. *Astron. J.* **1991**, *101*, 1632. [CrossRef]
14. Palmer, H.P.; Rowson, B.; Anderson, B.; Donaldson, W.; Miley, G.K. Radio Diameter Measurements with Interferometer Baselines of One Million and Two Million Wavelengths. *Nature* **1967**, *213*, 789–790. [CrossRef]
15. Reid, M.J.; Schmitt, J.H.M.M.; Owen, F.N.; Booth, R.S.; Wilkinson, P.N.; Shaffer, D.B.; Johnston, K.J.; Hardee, P.E. VLBI observations of the nucleus and jet of M 87. *Astrophys. J.* **1982**, *263*, 615–623. [CrossRef]
16. Kovalev, Y.Y.; Lister, M.L.; Homan, D.C.; Kellermann, K.I. The Inner Jet of the Radio Galaxy M87. *Astrophys. J.* **2007**, *668*, L27–L30.
17. Kuo, C.Y.; Asada, K.; Rao, R.; Nakamura, M.; Algaba, J.C.; Liu, H.B.; Inoue, M.; Koch, P.M.; Ho, P.T.P.; Matsushita, S.; et al. Measuring Mass Accretion Rate onto the Supermassive Black Hole in M87 Using Faraday Rotation Measure with the Submillimeter Array. *Astrophys. J.* **2014**, *783*, L33.
18. Kino, M.; Takahara, F.; Hada, K.; Akiyama, K.; Nagai, H.; Sohn, B.W. Magnetization Degree at the Jet Base of M87 Derived from the Event Horizon Telescope Data: Testing the Magnetically Driven Jet Paradigm. *Astrophys. J.* **2015**, *803*, 30.
19. Mertens, F.; Lobanov, A.P.; Walker, R.C.; Hardee, P.E. Kinematics of the jet in M 87 on scales of 100-1000 Schwarzschild radii. *A&A* **2016**, *595*, A54.
20. Walker, R.C.; Hardee, P.E.; Davies, F.B.; Ly, C.; Junor, W. The Structure and Dynamics of the Subparsec Jet in M87 Based on 50 VLBA Observations over 17 Years at 43 GHz. *Astrophys. J.* **2018**, *855*, 128.

21. Kim, J.Y.; Krichbaum, T.P.; Lu, R.S.; Ros, E.; Bach, U.; Bremer, M.; de Vicente, P.; Lindqvist, M.; Zensus, J.A. The limb-brightened jet of M87 down to the 7 Schwarzschild radii scale. *A&A* **2018**, *616*, A188.
22. Chael, A.; Narayan, R.; Johnson, M.D. Two-temperature, Magnetically Arrested Disc simulations of the jet from the supermassive black hole in M87. *Mon. Not. R. Astron. Soc.* **2019**, *486*, 2873–2895.
23. Meisenheimer, K.; Roeser, H.J.; Schloetelburg, M. The synchrotron spectrum of the jet in M87. *A&A* **1996**, *307*, 61.
24. Kim, J.Y.; Krichbaum, T.P.; Broderick, A.E.; Wielgus, M.; Blackburn, L.; Gómez, J.L.; Johnson, M.D.; Bouman, K.L.; Chael, A.; Akiyama, K.; et al. Event Horizon Telescope imaging of the archetypal blazar 3C 279 at an extreme 20 microarcsecond resolution. *A&A* **2020**, *640*, A69. [CrossRef]
25. Wardle, J.F.C.; Homan, D.C.; Ojha, R.; Roberts, D.H. Electron-positron jets associated with the quasar 3C279. *Nature* **1998**, *395*, 457–461. [CrossRef]
26. Hirotani, K.; Iguchi, S.; Kimura, M.; Wajima, K. Pair Plasma Dominance in the Parsec-Scale Relativistic Jet of 3C 345. *Astrophys. J.* **2000**, *545*, 100–106.
27. Marscher, A.P.; Jorstad, S.G.; Gómez, J.L.; McHardy, I.M.; Krichbaum, T.P.; Agudo, I. Search for Electron-Positron Annihilation Radiation from the Jet in 3C 120. *Astrophys. J.* **2007**, *665*, 232–236. [CrossRef]
28. Celotti, A.; Fabian, A.C. The kinetic power and luminosity of parsec-scale radio jets - an argument for heavy jets. *Mon. Not. R. Astron. Soc.* **1993**, *264*, 228–236. [CrossRef]
29. Event Horizon Telescope Collaboration; Akiyama, K.; Algaba, J.C.; Alberdi, A.; Alef, W.; Anantua, R.; Asada, K.; Azulay, R.; Baczko, A.K.; Ball, D.; et al. First M87 Event Horizon Telescope Results. VII. Polarization of the Ring. *Astrophys. J.* **2021**, *910*, L12.
30. Event Horizon Telescope Collaboration; Akiyama, K.; Algaba, J.C.; Alberdi, A.; Alef, W.; Anantua, R.; Asada, K.; Azulay, R.; Baczko, A.K.; Ball, D.; et al. First M87 Event Horizon Telescope Results. VIII. Magnetic Field Structure near The Event Horizon. *Astrophys. J.* **2021**, *910*, L13.
31. Breit, G.; Wheeler, J.A. Collision of Two Light Quanta. *Phys. Rev.* **1934**, *46*, 1087–1091. [CrossRef]
32. Beskin, V.S.; Istomin, Y.N.; Parev, V.I. Filling the Magnetosphere of a Supermassive Black-Hole with Plasma. *Soviet Astron.* **1992**, *36*, 642.
33. Hirotani, K.; Okamoto, I. Pair Plasma Production in a Force-free Magnetosphere around a Supermassive Black Hole. *Astrophys. J.* **1998**, *497*, 563–572. [CrossRef]
34. Ford, A.L.; Keenan, B.D.; Medvedev, M.V. Electron-positron cascade in magnetospheres of spinning black holes. *Phys. Rev. D* **2018**, *98*, 063016.
35. Levinson, A.; Cerutti, B. Particle-in-cell simulations of pair discharges in a starved magnetosphere of a Kerr black hole. *A&A* **2018**, *616*, A184.
36. Chen, A.Y.; Yuan, Y.; Yang, H. Physics of Pair Producing Gaps in Black Hole Magnetospheres. *Astrophys. J.* **2018**, *863*, L31.
37. Parfrey, K.; Philippov, A.; Cerutti, B. First-Principles Plasma Simulations of Black-Hole Jet Launching. *Phys. Rev. Lett.* **2019**, *122*, 035101.
38. Mościbrodzka, M.; Gammie, C.F.; Dolence, J.C.; Shiokawa, H. Pair Production in Low-luminosity Galactic Nuclei. *Astrophys. J.* **2011**, *735*, 9.
39. Broderick, A.E.; Tchekhovskoy, A. Horizon-scale Lepton Acceleration in Jets: Explaining the Compact Radio Emission in M87. *Astrophys. J.* **2015**, *809*, 97.
40. Wong, G.N.; Ryan, B.R.; Gammie, C.F. Pair Drizzle around Sub-Eddington Supermassive Black Holes. *Astrophys. J.* **2021**, *907*, 73.
41. Ryan, B.R.; Dolence, J.C.; Gammie, C.F. General Relativistic Radiation Magnetohydrodynamics with Monte Carlo Transport. *Astrophys. J.* **2015**, *807*, 31. [CrossRef]
42. Ryan, B.R.; Ressler, S.M.; Dolence, J.C.; Tchekhovskoy, A.; Gammie, C.; Quataert, E. The Radiative Efficiency and Spectra of Slowly Accreting Black Holes from Two-temperature GRRMHD Simulations. *Astrophys. J.* **2017**, *844*, L24.
43. Ryan, B.R.; Ressler, S.M.; Dolence, J.C.; Gammie, C.; Quataert, E. Two-temperature GRRMHD Simulations of M87. *Astrophys. J.* **2018**, *864*, 126.
44. Wardle, J.F.C.; Homan, D.C. Theoretical Models for Producing Circularly Polarized Radiation in Extragalactic Radio Sources. *Astrophys. Space Sci.* **2003**, *288*, 143–153. [CrossRef]
45. Dexter, J. A public code for general relativistic, polarised radiative transfer around spinning black holes. *Mon. Not. R. Astron. Soc.* **2016**, *462*, 115–136.
46. Blandford, R.; Anantua, R. The Future of Black Hole Astrophysics in the LIGO-VIRGO-LPF Era. *J. Phys. Conf. Ser.* **2017**, *840*, 012023. [CrossRef]
47. McKinney, J.C.; Tchekhovskoy, A.; Blandford, R.D. General relativistic magnetohydrodynamic simulations of magnetically choked accretion flows around black holes. *Mon. Not. R. Astron. Soc.* **2012**, *423*, 3083–3117. [CrossRef]
48. Anantua, R.; Dúran, J.; Ngata, N.; Oramas, L.; Emami, R.; Ricarte, A.; Curd, B.; Röder, J.; Broderick, A.; Wayland, J.; et al. Emission Modeling in the EHT-ngEHT Age. *Galaxies* **2023**, *11*, 4.
49. Doeleman, S.S.; Weintroub, J.; Rogers, A.E.E.; Plambeck, R.; Freund, R.; Tilanus, R.P.J.; Friberg, P.; Ziurys, L.M.; Moran, J.M.; Corey, B.; et al. Event-horizon-scale structure in the supermassive black hole candidate at the Galactic Centre. *Nature* **2008**, *455*, 78–80. [CrossRef]
50. Doeleman, S.S.; Fish, V.L.; Schenck, D.E.; Beaudoin, C.; Blundell, R.; Bower, G.C.; Broderick, A.E.; Chamberlin, R.; Freund, R.; Friberg, P.; et al. Jet-Launching Structure Resolved Near the Supermassive Black Hole in M87. *Science* **2012**, *338*, 355. [CrossRef]

51. Prieto, M.A.; Fernández-Ontiveros, J.A.; Markoff, S.; Espada, D.; González-Martín, O. The central parsecs of M87: jet emission and an elusive accretion disc. *Mon. Not. R. Astron. Soc.* **2016**, *457*, 3801–3816. [CrossRef]
52. Prather, B.; Wong, G.; Dhruv, V.; Ryan, B.; Dolence, J.; Ressler, S.; Gammie, C. iharm3D: Vectorized General Relativistic Magnetohydrodynamics. *J. Open Source Softw.* **2021**, *6*, 3336. [CrossRef]
53. Ricarte, A.; Qiu, R.; Narayan, R. Black hole magnetic fields and their imprint on circular polarization images. *Mon. Not. R. Astron. Soc.* **2021**, *505*, 523–539.
54. Mościbrodzka, M.; Gammie, C.F. IPOLE - semi-analytic scheme for relativistic polarized radiative transport. *Mon. Not. R. Astron. Soc.* **2018**, *475*, 43–54.